

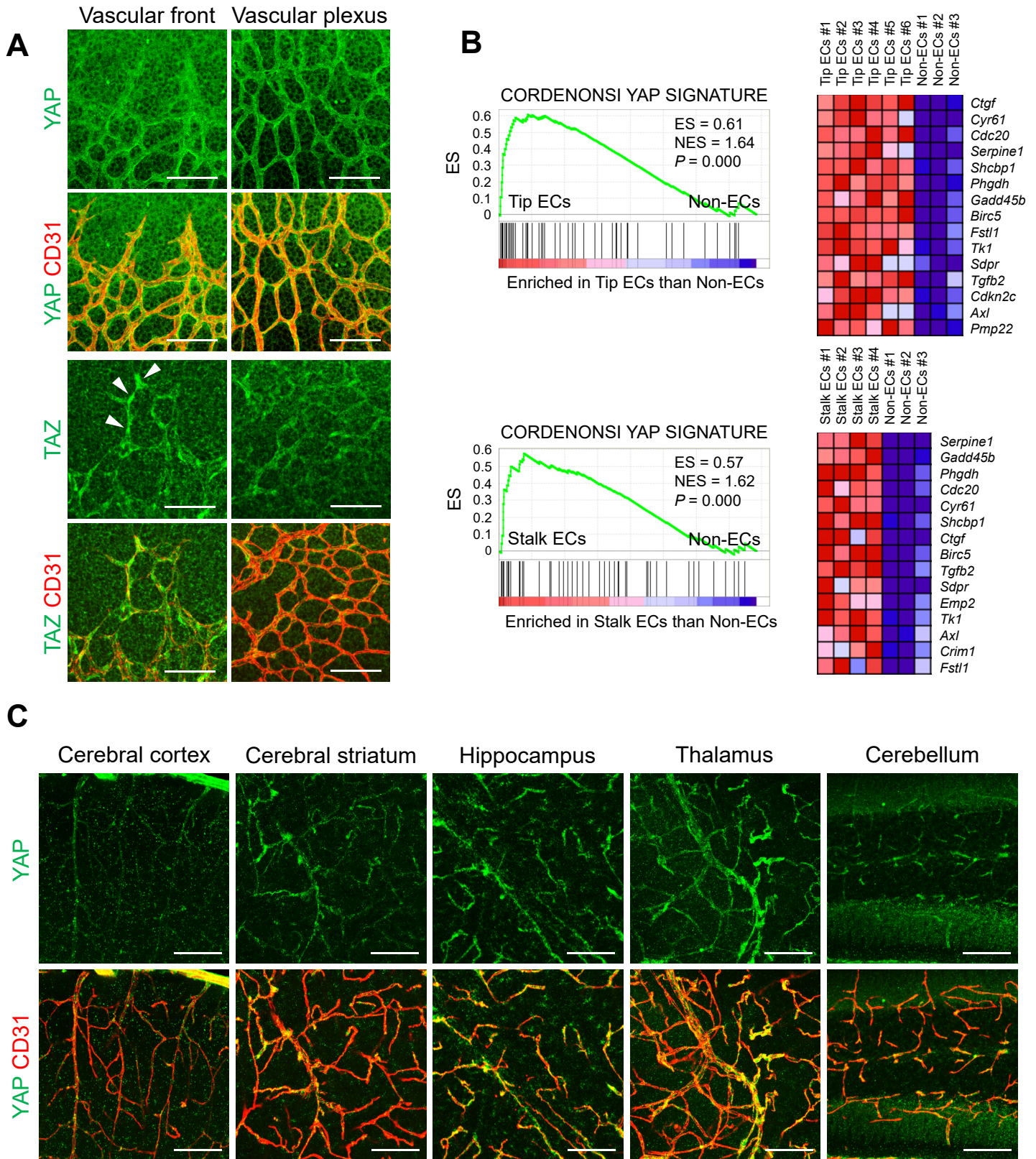
[Supplemental data](#)

YAP/TAZ regulates sprouting angiogenesis and vascular barrier maturation

Jongshin Kim, Yoo Hyung Kim, Jaeryung Kim, Do Young Park, Hosung Bae,
Da-Hye Lee, Kyun Hoo Kim, Seon Pyo Hong, Seung Pil Jang, Yoshiaki Kubota, Young-Guen
Kwon, Dae-Sik Lim, Gou Young Koh

It includes;

1. Supplementary Figures 1-9 and their legends
2. Supplementary Tables 1-3
3. Supplementary Methods



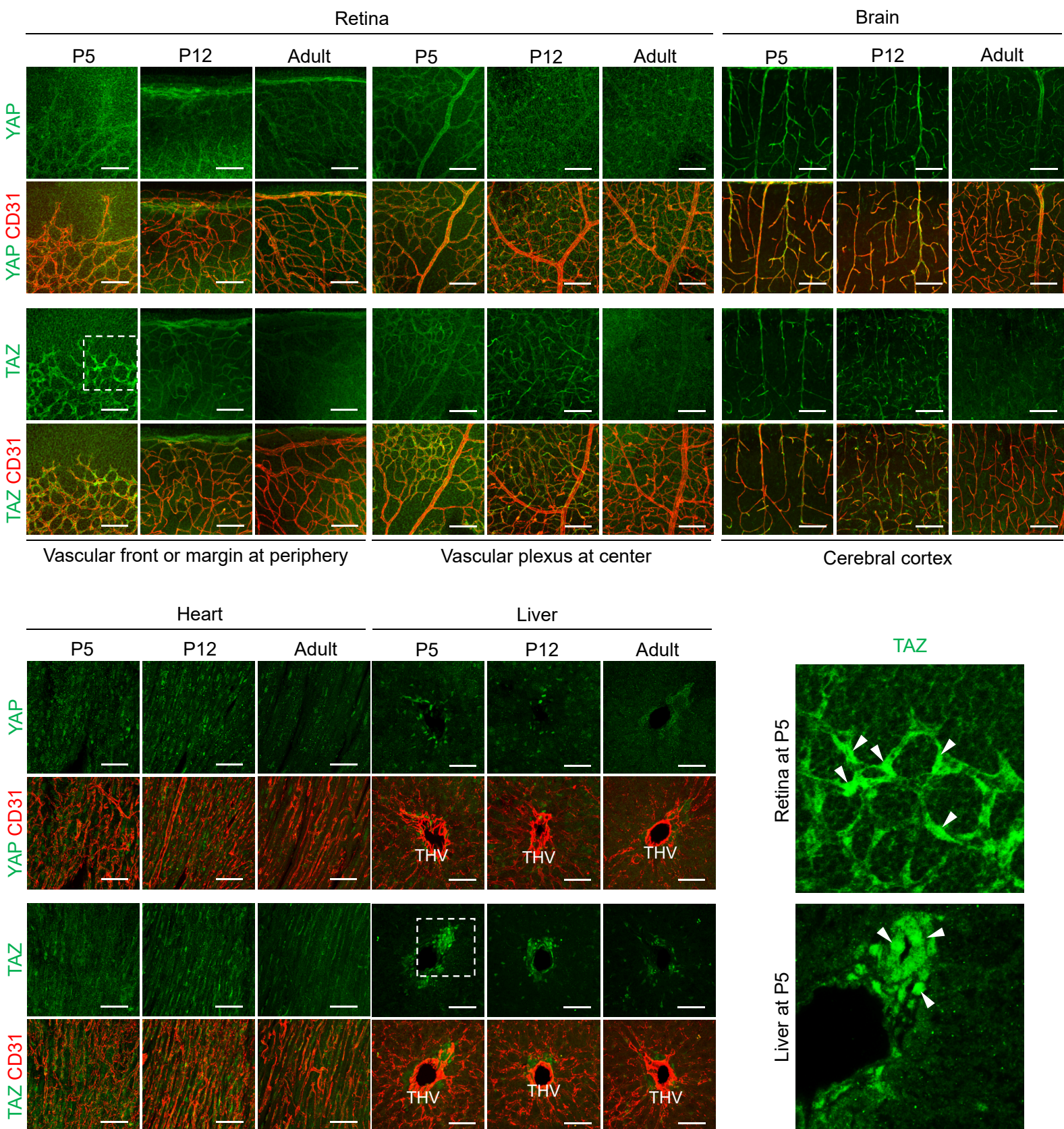
Supplementary Figure 1. Expressions of YAP and its target genes in retinal and brain endothelium at postnatal period. (A) Images of distributions of YAP, TAZ and CD31⁺ vessels in mouse retina at P5.

Note that TAZ is highly distributed in the nuclei in both tip and stalk ECs (white arrowheads) . Scale bar: 100 μ m.

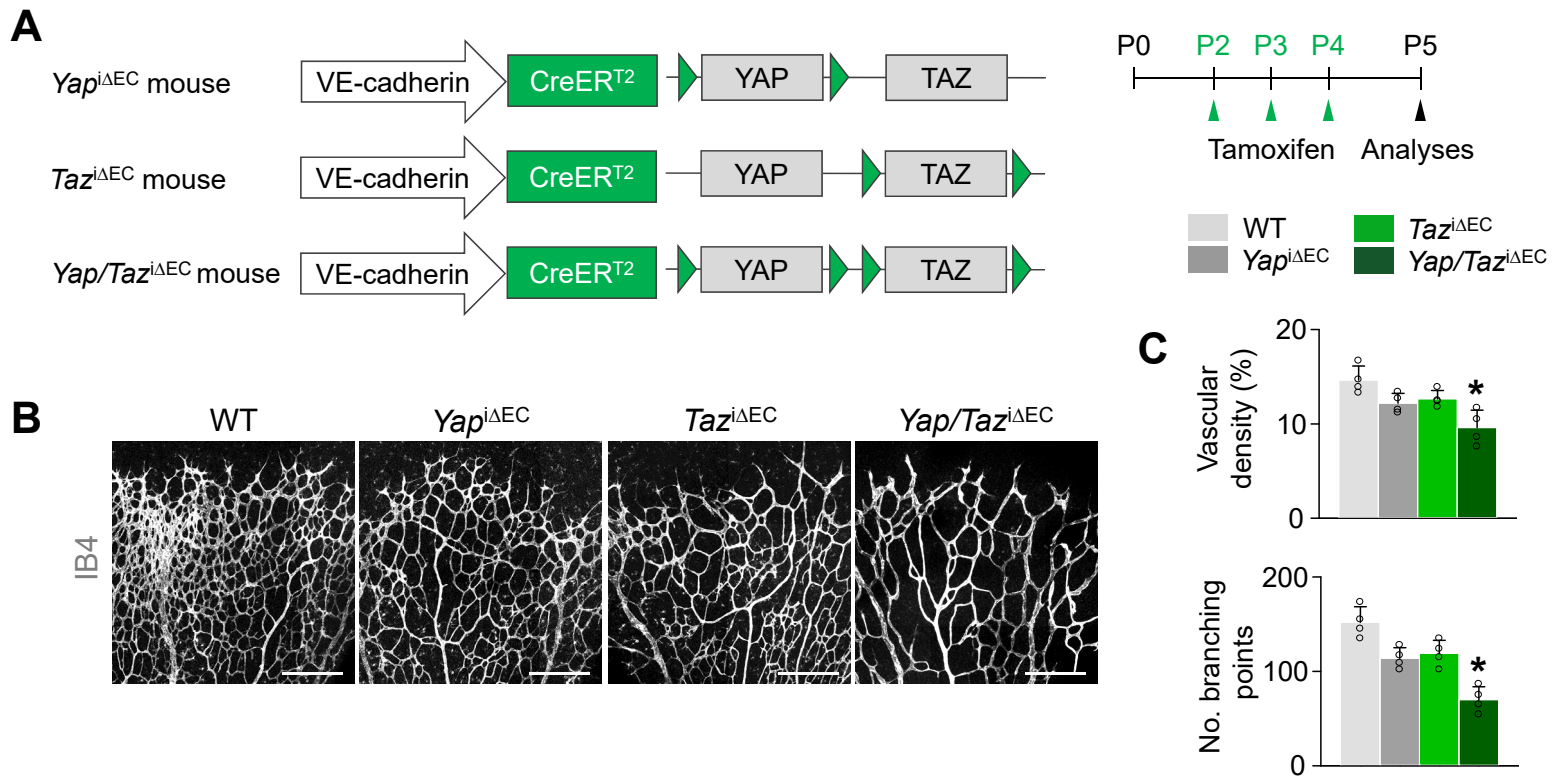
(B) GSEA of the microarray data (GSE19284) obtained from isolated tip ECs, stalk ECs, and non-ECs by using laser capture microdissection. Note that YAP and its target genes are enriched in tip ECs or stalk ECs compared with non-ECs. ES, enrichment score; NES, normalized enrichment score.

(C) Images of distribution of YAP and CD31⁺ vessels in indicated regions of mouse brain at P5. Scale bar: 100 μ m.

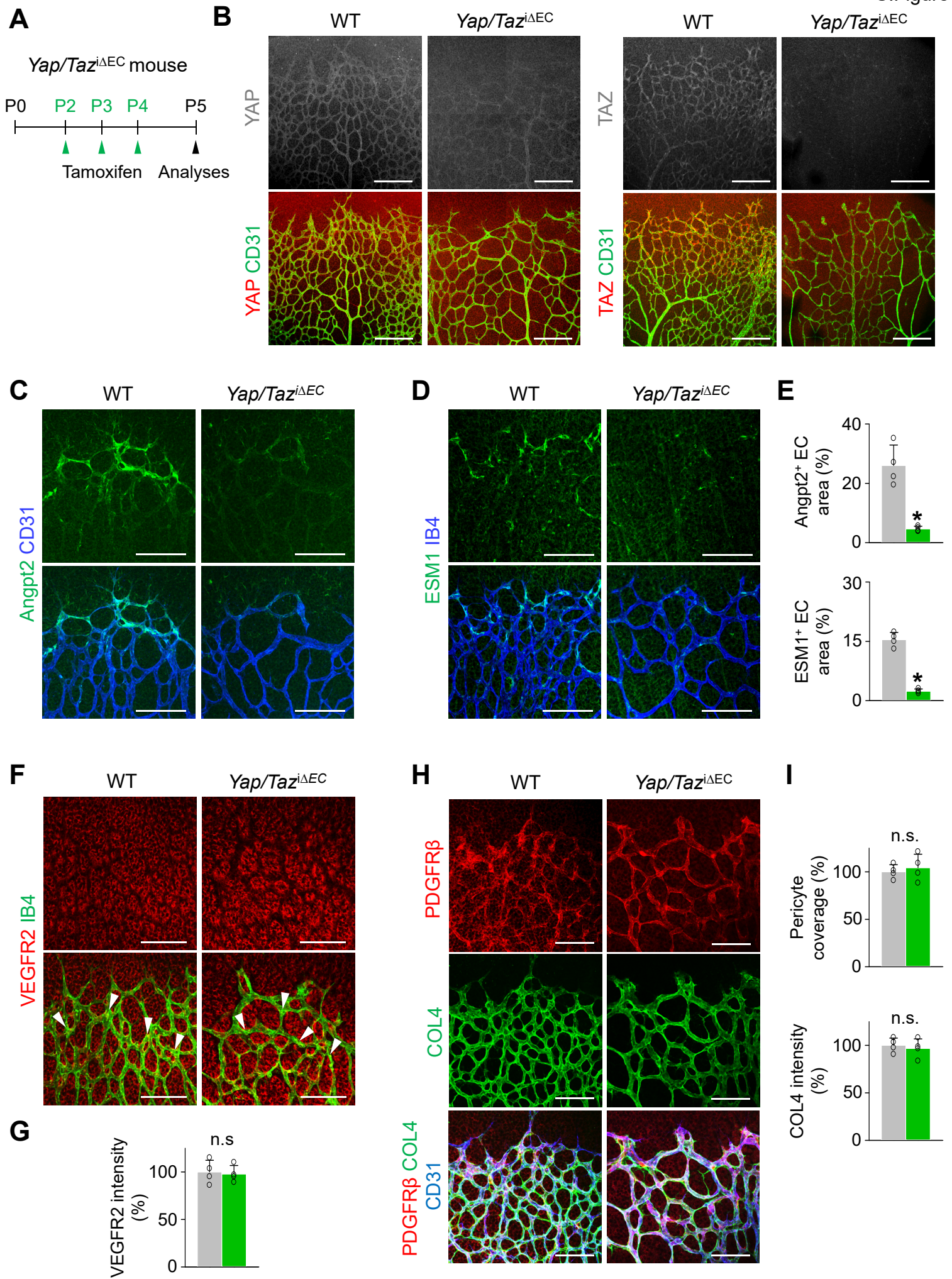
ES, enrichment score; NES, normalized enrichment score.



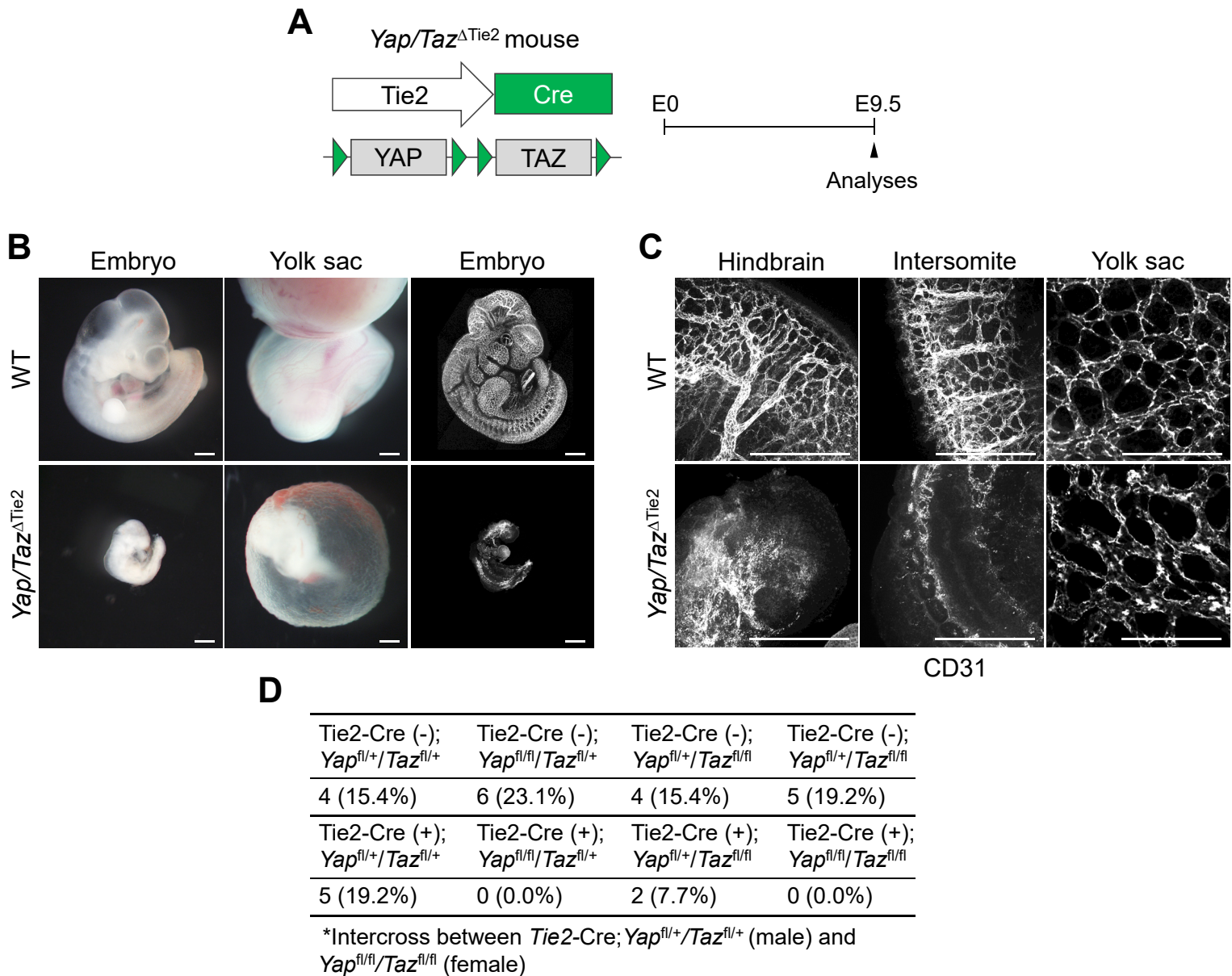
Supplementary Figure 2. Expressions of YAP and TAZ in retina, brain, heart and liver. Images of distributions of YAP, TAZ and CD31⁺ vessels in the vascular front and peripheral vascular margin of retina, cerebral cortex of brain, ventricular muscle of heart, and terminal hepatic venule (THV) region of liver at P5, P12 and adulthood. Scale bar: 100 μ m (upper panels), 50 μ m (lower panels). Note that YAP and TAZ are highly distributed in the ECs of blood vessels in retina and brain at P5 and P12, while they are highly distributed in the nuclei of non-ECs in heart and liver at P5 and P12. Magnified views of two dotted-line boxes are shown in right lower panels. Note that TAZ is highly distributed in the nuclei of ECs at retinal vascular front and non-ECs in liver at P5 (white arrowheads). Three different experiments have shown similar findings.



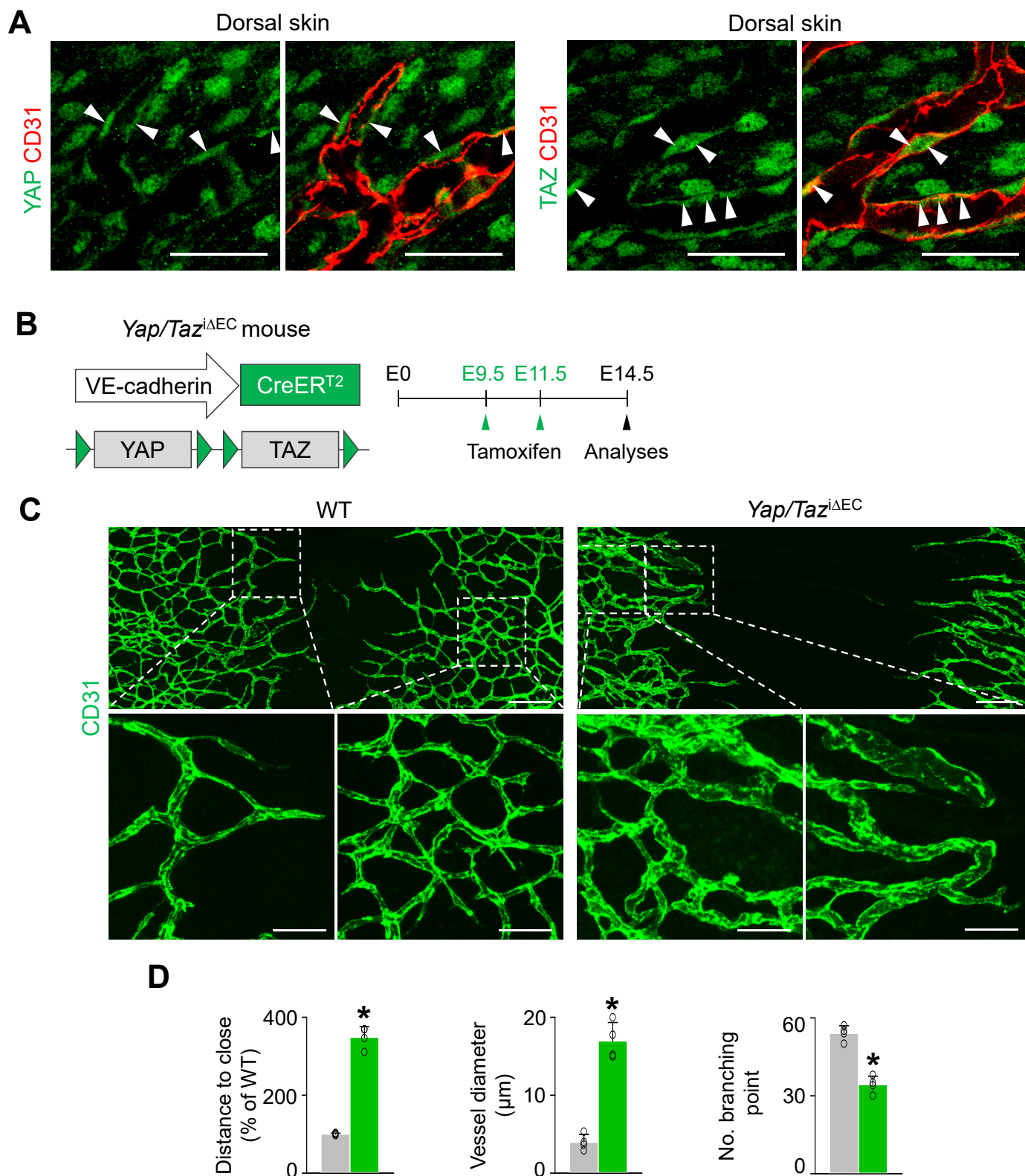
Supplementary Figure 3. Endothelial YAP and TAZ have overlapping roles in vascular growth. (A) Diagram for EC-specific deletions of YAP, TAZ and YAP/TAZ in retinal vessels from P2 and their analyses at P5 in *Yap*^{iΔEC}, *Taz*^{iΔEC} and *Yap/Taz*^{iΔEC} mice. (B and C) Images of IB4⁺ retinal vessels in indicated mice and comparisons of indicated parameters (n = 4, each group). Scale bar: 200 μm. Error bars represent mean ± s.d. **P* < 0.05 versus WT by Mann-Whitney *U* test.



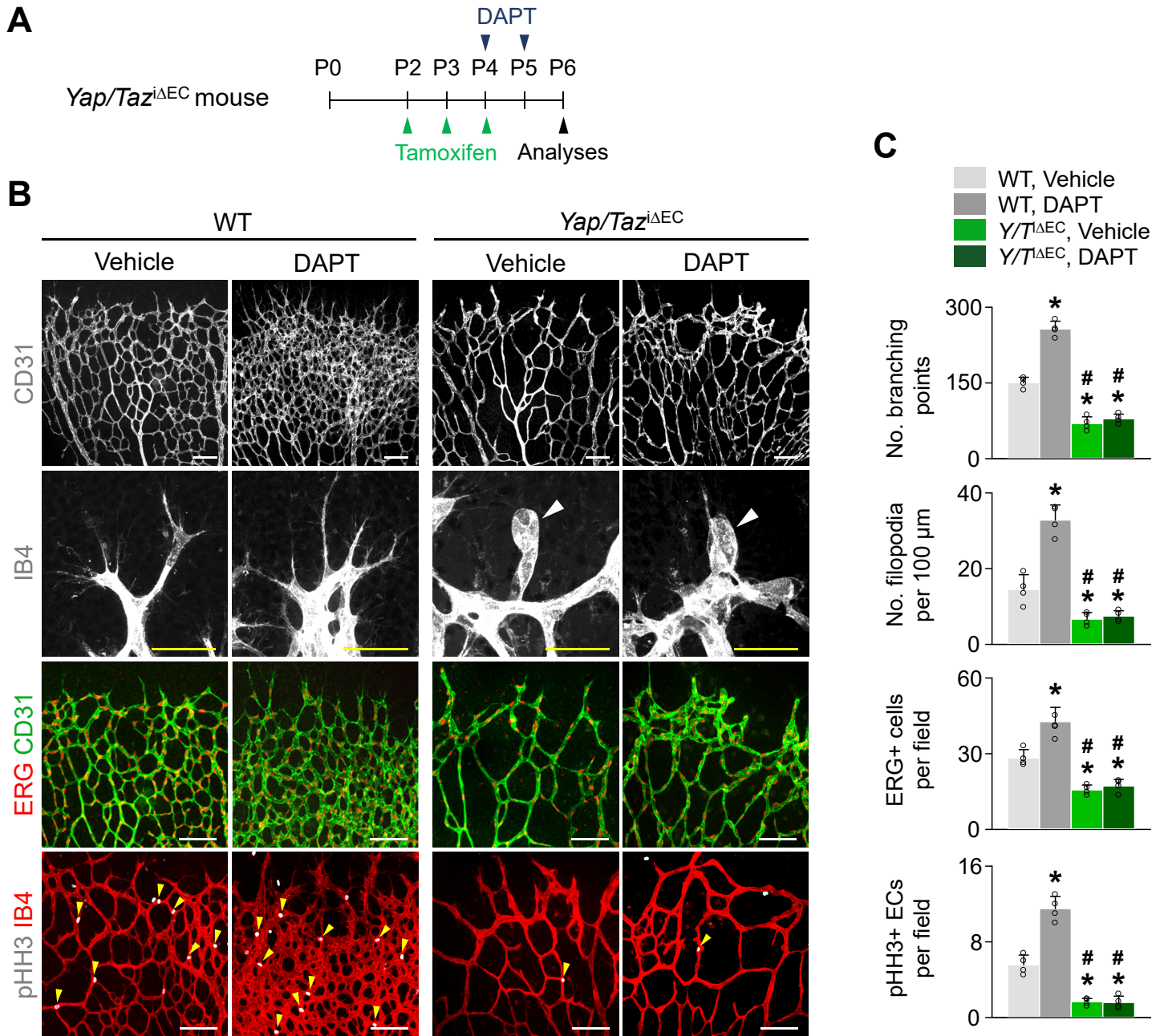
Supplementary Figure 4. Endothelial YAP/TAZ deletion reduces the expressions of Angpt2 and ESM1, tip cell markers , but does not affect pericyte coverage. (A) Diagram for EC-specific deletion of YAP/TAZ in retinal vessels from P2 and their analyses at P5 in *Yap/Taz*^{iΔEC} mice. **(B)** Images of distributions of YAP and TAZ in retinas at P5 in WT and *Yap/Taz*^{iΔEC} mice. Scale bar: 200 μm. **(C-E)** Images and comparisons of levels of Angpt2 and ESM1 in CD31⁺/IB4⁺ retinal vessels in WT and *Yap/Taz*^{iΔEC} mice (n = 4, each group). Scale bar: 100 μm. **(F and G)** Images and comparisons of level of VEGFR2 in IB4⁺ retinal vessels (white arrowheads) in WT and *Yap/Taz*^{iΔEC} mice (n = 4, each group). Scale bar: 100 μm. **(H and I)** PDGFRβ⁺ pericyte coverage and level of COL4⁺ on CD31⁺ retinal vessels of WT and *Yap/Taz*^{iΔEC} mice (n = 4, each group). Scale bar: 100 μm. Error bars represent mean ± s.d. **P* < 0.05 versus WT by Mann-Whitney *U* test. n.s., not significant.



Supplementary Figure 5. Endothelial YAP/TAZ is indispensable for angiogenesis during embryonic development. (A) Diagram for EC-specific deletion of YAP/TAZ and their analyses at E9.5 in *Yap/Taz*^{ΔTie2} mice. (B) Gross morphology of embryo proper and yolk sac, and images of CD31⁺ vasculature of WT and *Yap/Taz*^{ΔTie2} embryos at E9.5. (C) Images of CD31⁺ vessels in hindbrain, intersomite and yolk sac of WT and *Yap/Taz*^{ΔTie2} embryos at E9.5. Scale bars: 500 μm. (D) Table of offspring viability from *Tie2-Cre*; *Yap*^{fl/+}/*TAZ*^{fl/+} (male) and *Yap*^{fl/fl}/*TAZ*^{fl/fl} (female) intercrosses.

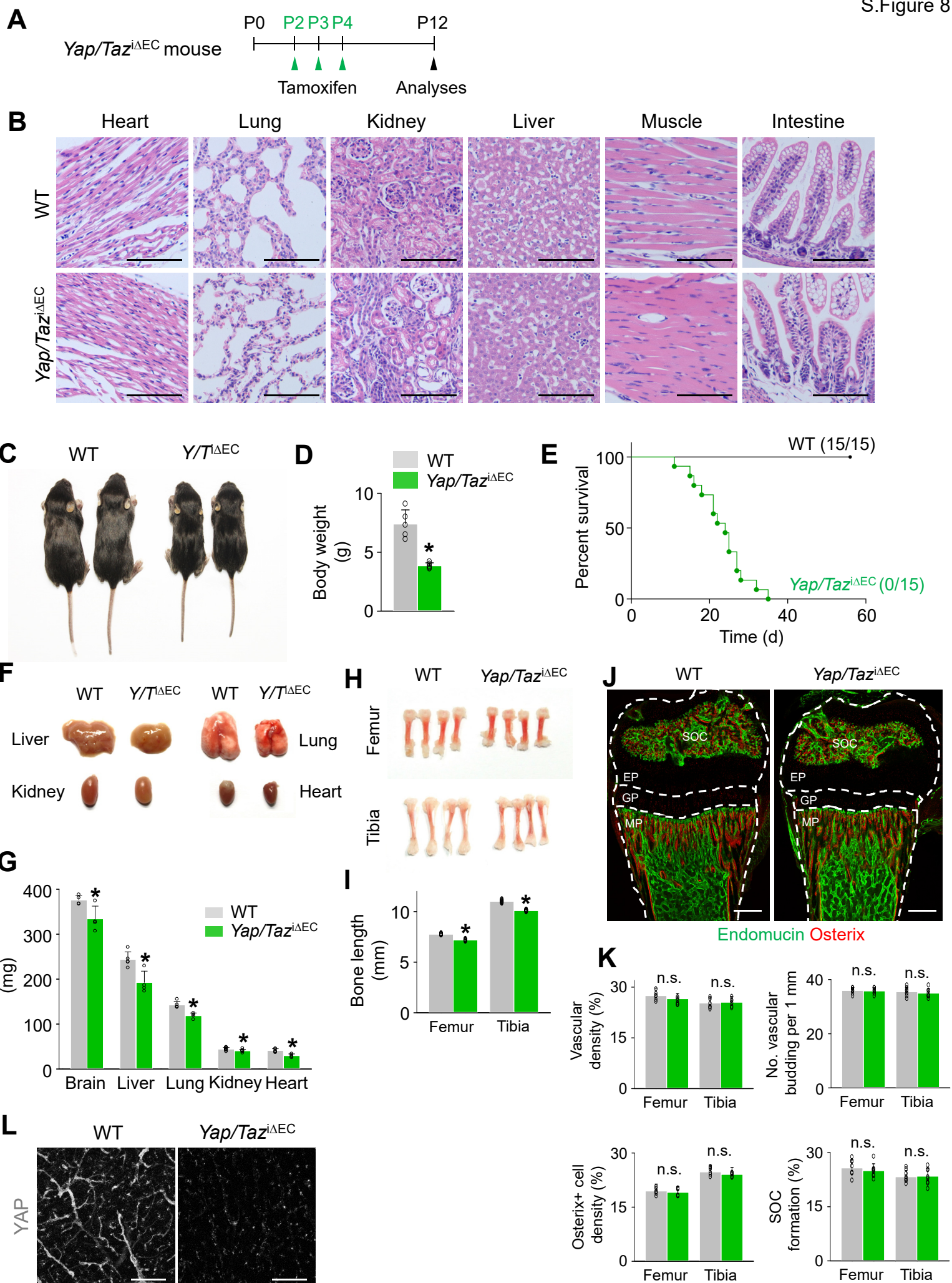


Supplementary Figure 6. Endothelial YAP/TAZ plays indispensable roles in angiogenesis in dorsal skin. (A) Images of distributions of YAP and TAZ in CD31⁺ vessels in mouse dorsal skin at E14.5. Scale bar: 50 μm. (B) Diagram for endothelial cell (EC)-specific deletion of YAP/TAZ from E9.5 and their analyses at E14.5 in *Yap/Taz*^{iΔEC} mice. (C and D) Images and comparisons of distance to close, vessel diameter and number of branching points in WT and *Yap/Taz*^{iΔEC} mice (n = 4, each group). Scale bar: 200 μm (upper panels); 100 μm (lower panels). Error bars represent mean ± s.d. *P < 0.05 versus WT by Mann-Whitney U test.

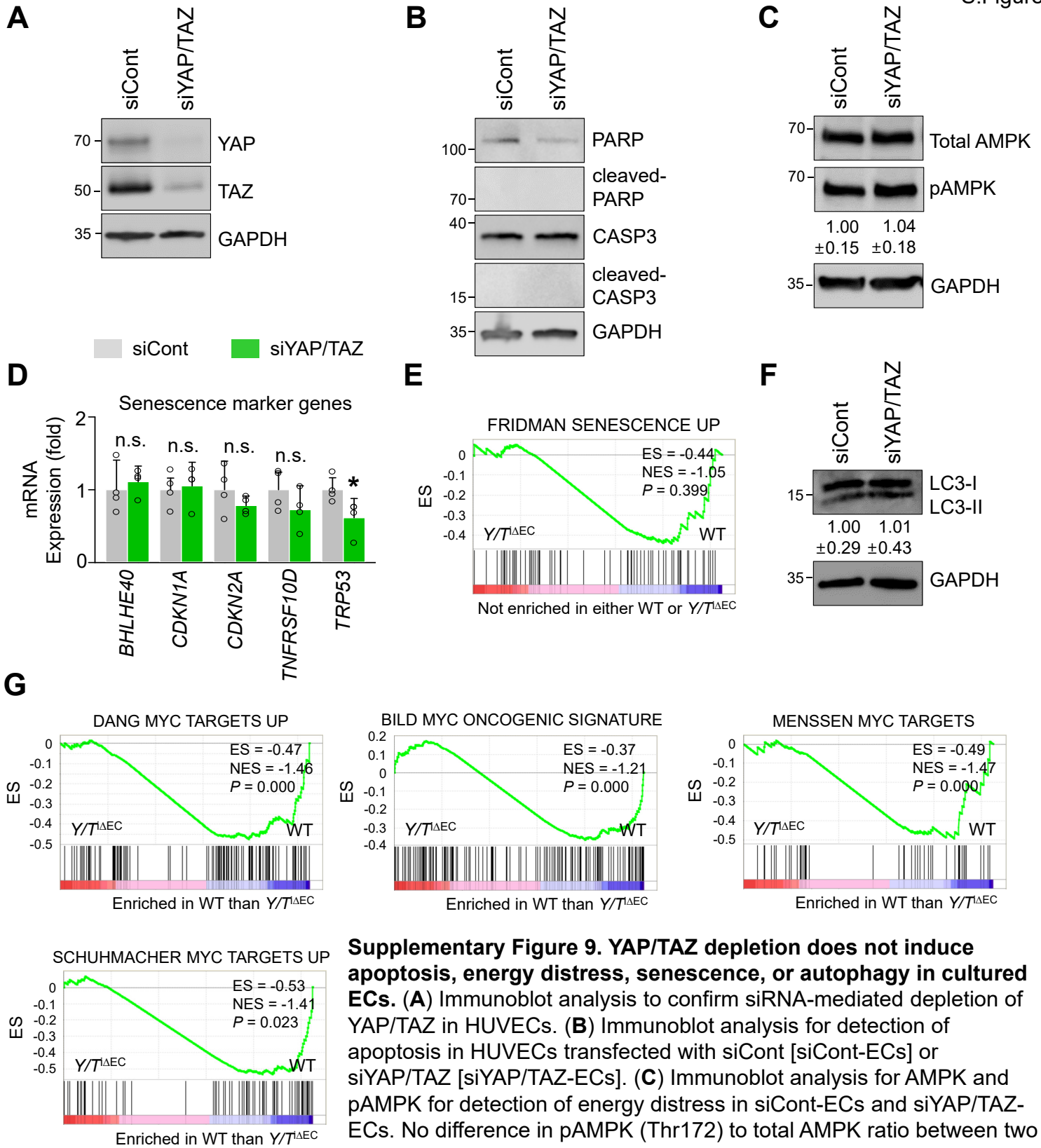


Supplementary Figure 7. Endothelial YAP/TAZ plays dominant roles in both tip cell formation and stalk cell proliferation

(A) Diagram depicting the experiment schedule for EC-specific deletion of YAP/TAZ from P2, intraperitoneal injection of DAPT at P4 and P5, and analyses of retinal vessels at P6 in *Yap/Taz*^{ΔEC} mice. (B and C) Images and comparisons of CD31⁺ and IB4⁺ retinal vessels, ERG⁺ ECs, and pHH3⁺ proliferative ECs (yellow arrowheads) in WT and *Yap/Taz*^{ΔEC} mice that were treated with vehicle (DMSO) or DAPT (n = 4, each group). Tip ECs of *Yap/Taz*^{ΔEC} mice treated with vehicle and DAPT both exhibited an aneurysm-like structure with less filopodia (white arrowheads). Scale bar: 100 μm. Error bars represent mean ± s.d. *P < 0.05 versus WT treated with vehicle, #P < 0.05 versus WT treated with DAPT by Mann-Whitney U test.



Supplementary Figure 8 . Endothelial YAP/TAZ deletion exhibits delayed growth and lethality during postnatal period. (A) Diagram depicting the experiment schedule for EC-specific deletion of YAP/TAZ in retinal vessels from P2 and their analyses at P12 in *Yap/Taz*^{iΔEC} mice. (B) H&E staining of indicated organs of WT and *Yap/Taz*^{iΔEC} mice. Scale bar: 100 μm. (C and D) Gross image and comparisons of body weight of WT and *Yap/Taz*^{iΔEC} mice (n = 4, each group). (E) Survival curve of WT and *Yap/Taz*^{iΔEC} mice (n = 15, each group). (F and G) Images of major organs and comparisons of organ weights in WT and *Yap/Taz*^{iΔEC} mice (n = 4, each group). (H and I) Images of femur and tibia and comparisons of their lengths in WT and *Yap/Taz*^{iΔEC} mice (n = 4, each group). (J and K) Images and comparisons of vascular density, number of vascular budding per 1 mm along the vascular front at the metaphysis-growth plate border, Osterix⁺ cell density of distal femur and formation of secondary ossification center (SOC) in WT and *Yap/Taz*^{iΔEC} mice (n = 4, each group). EP, epiphysis, GP, growth plate, MP, metaphysis. Scale bar: 200 μm. (L) Images of YAP protein in cerebral cortex of WT and *Yap/Taz*^{iΔEC} mice. Scale bar: 100 μm. Error bars represent mean ± s.d. **P* < 0.05 versus WT by Mann-Whitney *U* test. n.s., not significant.



Supplementary Figure 9. YAP/TAZ depletion does not induce apoptosis, energy distress, senescence, or autophagy in cultured ECs. (A) Immunoblot analysis to confirm siRNA-mediated depletion of YAP/TAZ in HUVECs. (B) Immunoblot analysis for detection of apoptosis in HUVECs transfected with siCont [siCont-ECs] or siYAP/TAZ [siYAP/TAZ-ECs]. (C) Immunoblot analysis for AMPK and pAMPK for detection of energy distress in siCont-ECs and siYAP/TAZ-ECs. No difference in pAMPK (Thr172) to total AMPK ratio between two groups is shown. (D) qPCR analysis of senescence-associated genes in siCont-ECs and siYAP/TAZ-ECs. (n = 4, each group). (E) GSEA of isolated brain ECs showing no significant enrichment of senescence signature genes between *Yap/Taz* Δ EC mice and WT mice. ES, enrichment score; NES, normalized enrichment score. (F) Immunoblot analysis for LC3-I and LC3-II for detection of autophagy in siCont-ECs and siYAP/TAZ-ECs. No difference in LC3-II to LC3-I ratio between two groups is shown. (G) GSEA of isolated brain ECs showing down-regulation of MYC signature genes in *Yap/Taz* Δ EC compared with WT mice. Error bars and numbers represent mean \pm s.d. * P < 0.05 versus siCont or WT mice by Mann-Whitney U test. n.s., not significant; ES, enrichment score; NES, normalized enrichment score.

Supplementary Table 1. GSEA of isolated brain ECs showing down-regulated gene sets related to metabolism in *Yap/Taz*^{iΔEC} mice compared with WT mice.

Annotated cellular function	Source	ES	NES	<i>P</i> value
YAP conserved signature	C6 (OS)	-0.50	-1.31	0.050
E2F targets	Hallmark	-0.44	-1.30	0.039
Glycolysis	Hallmark	-0.47	-1.41	0.000
Oxidative phosphorylation	Hallmark	-0.51	-1.65	0.000
Purine metabolism	C2:KEGG	-0.48	-1.38	0.000
Pyrimidine metabolism	C2:KEGG	-0.46	-1.32	0.035
MYC targets V1	Hallmark	-0.40	-1.36	0.028
MYC targets V2	Hallmark	-0.54	-1.40	0.000

Supplementary Table 2. List of Primer Sets for Quantitative Real-Time RT-PCR for mouse samples

Name		Sequence (5' - 3')
VEGF-A	Forward	CTCCACCATGCCAAGTGGTC
	Reverse	TCGTTACAGCAGCCTGCACA
CCL2	Forward	CCCAATGAGTAGGCTGGAGA
	Reverse	AAAATGGATCCACACCTTGC
CCL3	Forward	ACTGCCTGCTGCTTCTCCTACA
	Reverse	AGGAAAATGACACCTGGCTGG
Arginase1	Forward	CAGAAGAATGGAAGAGTCAG
	Reverse	CAGATATGCAGGGAGTCACC
Arginase2	Forward	TGATTGGCAAAGGCAGAGG
	Reverse	CTAGGAGTAGGAAGGTGGTC
TNF- α	Forward	CACGCTCTTCTGTCTACTGAACTTCG
	Reverse	GTGGGCTACAGGCTTGTCACTC
IL-6	Forward	TAGTCCTTCCTACCCCAATTTCC
	Reverse	TTGGTCCTTAGCCACTCCTTC
IL-10	Forward	GCTCTTACTGACTGGCATGAG
	Reverse	CGCAGCTCTAGGAGCATGTG
GAPDH	Forward	TGTTCTACCCCAATGTGT
	Reverse	TGTGAGGGAGATGCTCAGTG

Supplementary Table 3. List of Primer Sets for Quantitative Real-Time RT-PCR for human samples

Name		Sequence (5' - 3')
CTGF	Forward	AGGAGTGGGTGTGTGACGA
	Reverse	CCAGGCAGTTGGCTCTAATC
CYR61	Forward	CAGGACTGTGAAGATGCGGT
	Reverse	GCCTGTAGAAGGGAAACGCT
MYC	Forward	GGCTCCTGGCAAAGGTCA
	Reverse	CTGCGTAGTTGTGCTGATGT
BHLHE40	Forward	ATGAACCCAGACAAGATACCG
	Reverse	AAGCAAGGCAGCAGGAGA
CDKN1A	Forward	TGTCCGTCAGAACCCATGC
	Reverse	AAAGTCGAAGTTCCATCGCTC
CDKN2A	Forward	GATCCAGGTGGGTAGAAGGTC
	Reverse	CCCCTGCAAACCTTCGTCCT
TNFRSF10D	Forward	TACCACGACCAGAGACACC
	Reverse	CACCCTGTTCTACACGTCCG
TRP53	Forward	CCAGGGCAGCTACGGTTTC
	Reverse	CTCCGTCATGTGCTGTGACTG
GAPDH	Forward	GGTGGTCTCCTCTGACTTCAACA
	Reverse	GTTGCTGTAGCCAAATTCGTTGT

SUPPLEMENTAL METHODS

Histological analyses.

Immunofluorescence (IF) staining of whole-mounted retinas and retinal pigment epithelium (RPE)-choroid-sclera complexes were performed as previously described (1), and IF staining of sectioned bone tissues of femur and tibia was performed as previously described (2). Briefly, eyeballs were enucleated and fixed in 4% paraformaldehyde (PFA) for 20 min at room temperature (RT). After dissecting the retina or RPE-choroid-sclera complexes from eyeball, only retinas were additionally fixed in 1% PFA for 1 hr at RT. Then the samples were blocked with 5% donkey (or goat) serum in PBST (0.3% Triton X-100 in PBS) for 30 min, incubated in primary antibodies diluted in blocking solution at 4°C overnight, washed in PBST, and incubated in secondary antibodies in blocking solution at RT for 2 hr. The retinas were washed in PBST and mounted on microscope glass slides with Vectashield (Vector Laboratories, H-1200). For brain IF staining, mice were anesthetized and perfusion-fixed with 4% PFA. After dissecting the brain from skull, brains were additionally fixed in 4% PFA for 6 hr at 4°C. The brain samples were cut into 100- to 150- μ m sections by a vibratome (Leica, VT1200 S), immunostained, and mounted. IF staining of whole-mounted mouse embryo was performed as previously described (3). Primary antibodies and reagents used for IF were as follows: hamster anti-CD31 monoclonal (Millipore, MAB1398Z); isolectin B4 (IB4), Alexa Fluor 594-conjugated (Thermo Fisher Scientific, I21413); rabbit anti-YAP monoclonal (CST, #14074); rabbit anti-TAZ polyclonal (Sigma-Aldrich, HPA007415); rat anti-PDGFR β monoclonal (eBioscience, NC0091961); rabbit anti-GFAP polyclonal (DAKO, Z0334); Phalloidin, Alexa Fluor 488-conjugated (Thermo Fisher Scientific, A12379); rat anti-ICAM2 monoclonal (BD Pharmingen, 553326); rabbit anti-ERG monoclonal (Abcam, ab92513); rabbit anti-pHH3 polyclonal (Millipore, 05-806); rabbit anti-cleaved-caspase-3 (cl-CASP3) polyclonal (CST, #9664); human anti-Angpt2 monoclonal (clone 4H10) (3); goat anti-ESM1 polyclonal (R&D Systems, AF1999); rat anti-TER119 monoclonal (BD Pharmingen, 561033); rat anti-F4/80 monoclonal (eBioscience, 14-4801-81); rat anti-VE-cadherin monoclonal (BD Pharmingen, 555289); rabbit anti-ZO1 polyclonal (Thermo Fisher Scientific, 40-2200); mouse anti-Claudin-5, Alexa Fluor 488-conjugated monoclonal (Thermo

Fisher Scientific, 352588); goat anti-VEGFR2 polyclonal (R&D Systems, AF644); rat anti-PLVAP monoclonal (BD Biosciences, 553849); rabbit anti-GLUT1 polyclonal (EMD Millipore, 07-1401); rat anti-CD71 monoclonal (Bio-Rad, MCA1033GA); rabbit anti-collagen IV polyclonal (Bio-Rad, 2150-1470); rabbit anti-laminin polyclonal (Abcam, ab11575); rabbit anti-nidogen polyclonal (Abcam, ab14511); rat anti-perlecan monoclonal (EMD Millipore, MAB1948P); rabbit anti-phospho-MLC2 (at Ser19) polyclonal (CST, #3671); rabbit anti-Osterix polyclonal (SantaCruz, sc22536-R); rat anti-endomucin monoclonal (SantaCruz, sc-53941). After several washes, samples were incubated for 2 hr at RT with FITC-, Cy3-, or Cy5-conjugated streptavidin (BD pharmingen) or the following secondary antibodies: FITC-, Cy3-, or Cy5-conjugated anti-hamster IgG, anti-rat IgG, anti-rabbit IgG, anti-human IgG, and anti-goat IgG (Jackson ImmunoResearch). Images of all samples were obtained using a confocal microscope (Zeiss, LSM880) and processed with imaging softwares, ZEN (Zeiss) and Adobe Photoshop (Adobe). HUVECs were fixed in 4% PFA for 7 min at RT. After blocking, the cells were stained with primary and secondary antibodies using the same procedures as tissue staining, and mounted with DAKO mounting medium.

Morphometric analyses.

Morphometric measurement of retinas, brains, dorsal skins and bones were performed by using the ImageJ software (<http://rsb.info.nih.gov/ij>). Radial length of retinal vessels was measured as the distance from the optic disc to the peripheral vascular front in each leaflet of the retina and averaged. Retinal vascular density was measured as CD31⁺ or IB4⁺ retinal vessel area divided by total measured area of the retina and presented as a percentage. Number of branching point was measured manually in four 500 μm \times 500 μm fields located between an artery and a vein in each retina and averaged. Number of filopodia was normalized to a length of 100 μm along the angiogenic front, which was measured four times per sample and averaged. Filopodia length was examined in six 100 μm \times 100 μm areas of vascular front in each retina and averaged. Microaneurysm was defined as ballooning or outpouching of CD31⁺ or IB4⁺ retinal vessels and counted in six 200 μm \times 200 μm fields per retina and averaged. Vessel diameters were averaged among 10 consecutive CD31⁺ or IB4⁺ retinal vessels between an artery and a vein located within

500 μm from the optic disc. Number of ERG⁺ ECs were counted in six 200 μm \times 200 μm fields and averaged per sample. Number of pHH3⁺ proliferating ECs and CASP3⁺ apoptotic ECs were measured in four 500 μm \times 500 μm fields and averaged per sample. Pericyte coverage was calculated as PDGFR β ⁺ area divided by CD31⁺ or IB4⁺ area and averaged, which was then normalized by the average of those of control mice. RBC leakage were measured as RBC-stained area outside the vessels divided by retinal area. Macrophage infiltration was measured as F4/80⁺ area divided by retinal area. RBC leakage and macrophage infiltration were measured in six 200 μm \times 200 μm fields per retina and averaged. CNV volumes were measured from Z-stack images using imageJ software, which are presented as μm^3 . Staining intensities were measured in ten regions of interest (ROIs) of vessels or, if indicated, other vascular regions in each retina and averaged. For comparison, the values were subtracted by the background signals in non-vascularized areas and averaged, which were then normalized by the average of those of control and presented as fold change or percentage. Stained area of specific molecules in retinal vessels were measured using same threshold values in ImageJ software and divided by total area of CD31⁺ or IB4⁺ retinal vessels. Vascular density in brains was measured as CD31⁺ vessel area divided by total measured area of brain with Z-projected images of 100 μm -thickness and presented as a percentage. For other parameters, Z-projected images of 10 μm -thickness were used for the morphometric measurements of brain. Microaneurysm was counted in 850 μm \times 850 μm fields per fields per brain and averaged. The number of filopodia per tip cell and filopodia length was measured in 150 μm \times 150 μm fields per brain and averaged. Dextran leakage was quantified by subtracting vessel area from dextran⁺ area and then divided by brain area. Identical measurements of those performed with retina were employed for other morphometric analyses for brain. Distance to close of dorsal skin vessels was measured five times per sample as the distance between vascular fronts and dorsal midline and averaged. In the area located 1 mm away from dorsal midline, vessel diameters were averaged among 10 consecutive CD31⁺ dorsal skin vessels and number of branching points was measured manually in four 500 μm \times 500 μm fields. Vascular density and Osterix⁺ cell density were measured as endomucin⁺ vessel area and Osterix⁺ cell area, respectively, in the metaphysis divided by total measured area of the metaphysis and presented as a percentage. Number of vascular budding was measured manually

and normalized to a length of 1 mm along the vascular front at the metaphysis-growth plate border. Formation of secondary ossification center (SOC) was measured as endomucin⁺ vessel area in the epiphysis divided by total measured area of the epiphysis and presented as a percentage. Number of vascular budding and formation of SOC were measured four times per sample and averaged.

Immunoblotting.

For immunoblot analysis, cells were lysed on ice in RIPA lysis buffer supplemented with protease and phosphatase inhibitors (Roche). Cell lysates were centrifuged for 10 min at 4°C, 13,000 rpm. Protein concentrations of the supernatants were quantitated using the detergent-insensitive Pierce BCA protein assay kit (Thermo Scientific, 23227). Lamni buffer was added to total protein lysates and samples were denatured at 95°C for 5 min. Aliquots of each protein lysate (10-20 µg) were subjected to SDS-polyacrylamide gel electrophoresis. After electrophoresis, proteins were transferred to nitrocellulose membranes and blocked for 30 min with 5% skim milk in TBST (0.1% Tween 20 in TBS). For phosphorylated protein detection, membranes were blocked with 2% BSA in TBS. Primary antibodies were incubated overnight at 4 °C. After washes, membranes were incubated with anti-rabbit (CST, #7074) or anti-mouse (CST, #7076) secondary peroxidase-coupled antibody for 1 hr at RT. Target proteins were detected using ECL western blot detection solution (Millipore, WBKLS0500). Primary antibodies used for immunoblotting were as follows: mouse anti-YAP monoclonal (SantaCruz, sc-101199); rabbit anti-phospho-YAP (at Ser127) polyclonal (CST, #4911); rabbit anti-LATS1 monoclonal (CST, #3477); rabbit anti-phospho-LATS1 (at Thr1079) monoclonal (CST, #8654); rabbit anti-VEGFR2 monoclonal (CST, #2479); rabbit anti-phospho-VEGFR2 monoclonal (CST, #2478); rabbit anti-AKT polyclonal (CST, #9272); rabbit anti-phospho-AKT monoclonal (CST, #4058); rabbit anti-ERK monoclonal (CST, #4695); rabbit anti-phospho-ERK monoclonal (CST, #4376); rabbit anti-eNOS monoclonal (CST, #5880); rabbit anti-phospho-eNOS monoclonal (CST, #9570); rabbit anti-PAK2 monoclonal (CST, #2615); rabbit anti-phospho-PAK2 polyclonal (CST, #2606); rabbit anti-FAK polyclonal (SantaCruz, sc-558); rabbit anti-phospho-FAK polyclonal (CST, #3283); rabbit anti-CDC42 polyclonal (CST, #2462); rabbit anti-RAC1/2/3 polyclonal (CST, #2465); rabbit anti-RHOA

monoclonal (CST, #2117); rabbit anti-MLC2 polyclonal (CST, #3672S); rabbit anti-phospho-MLC2 (at Ser19) polyclonal (CST, #3671); rabbit anti-MYH9 polyclonal (CST, #3403); rabbit anti-MYH10 monoclonal (CST, #8824); rabbit anti-c-MYC (MYC) polyclonal (CST, #9402); rabbit anti-PARP monoclonal (CST, #9532); rabbit anti-cleaved-PARP monoclonal (CST, #5625); rabbit anti-Caspase3 (CASP3) polyclonal (CST, #9662); rabbit anti-cleaved-Caspase3 (cl-CASP3) monoclonal (CST, #9664); rabbit anti-AMPK polyclonal (CST, #2532); rabbit anti-phospho-AMPK monoclonal (CST, #2535); rabbit anti-LC3A/B monoclonal (CST, #12741); rabbit anti-GAPDH monoclonal (CST, #5174).

RNA extraction and quantitative RT-PCR.

Total RNA was extracted from samples using RNeasy mini kit (Qiagen) according to the manufacturer's protocols. A total of 1 µg of extracted RNA was transcribed into cDNA using GoScript™ Reverse Transcription System (Promega). cDNA was mixed with primers and FastStart SYBR Green Master (Roche), and mRNA expression levels were measured by real-time qRT-PCR on CFX96 system (Bio-Rad). The primers were designed using Primer-BLAST or adopted from previously published studies. The list of qRT-PCR primers used in this study is described in Supplemental Table 2 and 3. Primer reaction specificity was confirmed by melting curve analysis. Relative gene expression was analyzed by $\Delta\Delta C_t$ method using the CFX Manager software (Bio-Rad).

Transcriptional profile analysis of microarray data.

Expression data from the published studies were obtained from the Gene Expression Omnibus [<http://www.ncbi.nlm.nih.gov/geo>; accession number GSE19284 (4) and GSE18913 (5)]. GSEA was performed with the YAP target gene signature (6) and the results which were < 0.05 nominal P -value were stated.

SUPPLEMENTAL REFERENCES

1. Lee J, Kim KE, Choi D-K, Jang JY, Jung J-J, Kiyonari H, et al. Angiopoietin-1 guides directional angiogenesis through integrin $\alpha v\beta 5$ signaling for recovery of ischemic retinopathy. *Sci Trans Med*. 2013;5(203):203ra127.
2. Kusumbe AP, Ramasamy SK, Starsichova A, and Adams RH. Sample preparation for high-resolution 3D confocal imaging of mouse skeletal tissue. *Nat Protoc*. 2015;10(12):1904-1914.
3. Han S, Lee SJ, Kim KE, Lee HS, Oh N, Park I, et al. Amelioration of sepsis by TIE2 activation-induced vascular protection. *Sci Transl Med*. 2016;8(335):335ra55.
4. Strasser GA, Kaminker JS, and Tessier-Lavigne M. Microarray analysis of retinal endothelial tip cells identifies CXCR4 as a mediator of tip cell morphology and branching. *Blood*. 2010;115(24):5102-5110.
5. Suehiro J, Hamakubo T, Kodama T, Aird WC, and Minami T. Vascular endothelial growth factor activation of endothelial cells is mediated by early growth response-3. *Blood*. 2010;115(12):2520-2532.
6. Cordenonsi M, Zanconato F, Azzolin L, Forcato M, Rosato A, Frasson C, et al. The Hippo transducer TAZ confers cancer stem cell-related traits on breast cancer cells. *Cell*. 2011;147(4):759-772.